Astronomy & Astrophysics

Special issue

Sausage, kink, and fluting magnetohydrodynamic wave modes identified in solar magnetic pores by Solar Orbiter/PHI[*]

S. Jafarzadeh[1], L. A. C. A. Schiavo[2,3], V. Fedun[4], S. K. Solanki[1], M. Stangalini[5], D. Calchetti[1],
G. Verth[6], D. B. Jess[7,8], S. D. T. Grant[7], I. Ballai[6], R. Gafeira[9], P. H. Keys[7], B. Fleck[10], R. J. Morton[3],
P. K. Browning[2], S. S. A. Silva[4], T. Appourchaux[11], A. Gandorfer[1], L. Gizon[1,14], J. Hirzberger[1], F. Kahil[1],
D. Orozco Suárez[12], J. Schou[1], H. Strecker[12], J. C. del Toro Iniesta[12], G. Valori[1],
R. Volkmer[13], and J. Woch[1]

[1] Max Planck Institute for Solar System Research, Justus-von-Liebig-Weg 3, 37077 Göttingen, Germany
e-mail: shahin.jafarzadeh@mps.mpg.de
[2] School of Physics & Astronomy, The University of Manchester, Oxford Road, M13 9PL Manchester, UK
[3] Department of Mathematics, Physics and Electrical Engineering, Northumbria University, Newcastle upon Tyne NE1 8ST, UK
[4] Plasma Dynamics Group, Department of Automatic Control and Systems Engineering, The University of Sheffield, Mappin Street, Sheffield S1 3JD, UK
[5] ASI Italian Space Agency, Via del Politecnico snc, 00133 Rome, Italy
[6] Plasma Dynamics Group, School of Mathematics and Statistics, The University of Sheffield, Hicks Building, Hounsfield Road, Sheffield S3 7RH, UK
[7] Astrophysics Research Centre, School of Mathematics and Physics, Queen's University Belfast, Belfast BT7 1NN, UK
[8] Department of Physics and Astronomy, California State University Northridge, Northridge, CA 91330, USA
[9] Instituto de Astrofísica e Ciências do Espaço, Department of Physics, University of Coimbra, 3040-004 Coimbra, Portugal
[10] ESA Science and Operations Department, c/o NASA Goddard Space Flight Center, Greenbelt, MD 20771, USA
[11] Univ. Paris-Sud, Institut d'Astrophysique Spatiale, UMR 8617, CNRS, Bâtiment 121, 91405 Orsay Cedex, France
[12] Instituto de Astrofísica de Andalucá (IAA-CSIC), Apartado de Correos 3004, 18080 Granada, Spain
[13] Leibniz-Institut für Sonnenphysik, Schöneckstr. 6, 79104 Freiburg, Germany
[14] Institut für Astrophysik und Geophysik, Georg-August-Universität Göttingen, Friedrich-Hund-Platz 1, 37077 Göttingen, Germany

ABSTRACT

Solar pores are intense concentrations of magnetic flux that emerge through the solar photosphere. When compared to sunspots, they are much smaller in diameter and can therefore be affected and buffeted by neighbouring granular activity to generate significant magnetohydrodynamic (MHD) wave energy flux within their confines. However, observations of solar pores from ground-based telescope facilities may struggle to capture subtle motions that are synonymous with higher-order MHD wave signatures because of the seeing effects that are produced in the Earth's atmosphere. Hence, we exploited timely seeing-free and high-quality observations of four small magnetic pores from the High Resolution Telescope (HRT) of the Polarimetric and Helioseismic Imager (PHI) on board the Solar Orbiter spacecraft during its first close perihelion passage in March 2022 (at a distance of 0.5 au from the Sun). Through acquisition of data under stable observing conditions, we were able to measure the area fluctuations and horizontal displacements of the solar pores. Cross correlations between perturbations in intensity, area, line-of-sight velocity, and magnetic fields, coupled with the first-time application of novel proper orthogonal decomposition techniques on the boundary oscillations, provided a comprehensive diagnosis of the embedded MHD waves as sausage and kink modes. Additionally, the previously elusive $m = 2$ fluting mode is identified in the most magnetically isolated of the four pores. An important consideration lies in how the identified wave modes contribute to the transfer of energy into the upper solar atmosphere. Approximately 56%, 72%, 52%, and 34% of the total wave energy of the four pores we examined is associated with the identified sausage modes and about 23%, 17%, 39%, and 49% with their kink modes, while the first pore also receives a contribution of about 11% linked to the fluting mode. This study reports the first-time identification of concurrent sausage, kink, and fluting MHD wave modes in solar magnetic pores.

Key words. magnetohydrodynamics (MHD) – Sun: magnetic fields – Sun: oscillations – Sun: photosphere

1. Introduction

Theoretical models have suggested the existence of a large number of magnetohydrodynamic (MHD) wave modes in the same magnetic structures in the solar atmosphere (Edwin & Roberts 1983; Nakariakov & Verwichte 2005; Roberts 2019), each

of which can contribute to the heating of its outer layers (Jess et al. 2015; Khomenko & Collados 2015; Houston et al. 2020; Gilchrist-Millar et al. 2021). The identification of different MHD wave modes is therefore essential for a better understanding of the energy budget of the upper atmosphere (see, e.g. Jess et al. 2023, and references therein). MHD waves are often generated in the low photosphere in a variety of magnetic field concentrations (on different spatial scales), and they subsequently propagate into the upper solar atmosphere along

---

[*] Movies associated to Fig. 8 are available at https://www.aanda.org

the field lines (e.g. Jefferies et al. 2006; Stangalini et al. 2011; Morton et al. 2013; Jafarzadeh et al. 2017c; Bate et al. 2022).

Multiple MHD wave modes have only recently been identified in relatively large solar magnetic structures, such as pores and sunspots, through sophisticated analysis approaches, such as k-ω filtering (Tarbell et al. 1988; Title et al. 1989; Rutten & Krijger 2003; Jess et al. 2017), B-ω analysis (Stangalini et al. 2021c), and solar applications of proper orthogonal decomposition (POD) and dynamic mode decomposition (DMD) techniques (Albidah et al. 2021) applied to high-resolution observations. The results were interpreted together with theoretical and/or numerical models (see also Stangalini et al. 2022; Albidah et al. 2022, 2023). These studies have often concentrated on oscillations in intensity, line-of-sight (LOS) velocity, and polarisation signals within the magnetic structures (Stangalini et al. 2018, 2021a; Jess et al. 2020; Grant et al. 2022). Additionally, the area perturbations as a measure of MHD sausage modes (Erdélyi & Morton 2009; Moreels & Van Doorsselaere 2013; Moreels et al. 2013) have also been explored in a few studies of sunspots and pores in photospheric time-series of intensity images (e.g. Dorotovič et al. 2014; Moreels et al. 2015; Freij et al. 2016; Feng et al. 2020). By employing empirical decomposition methods on time variations of the size of magnetic pores, Morton et al. (2011) found multiple signatures of magnetoacoustic sausage modes with periods in the range of 30–450 s. Later, Grant et al. (2015) reported the detection of upward-propagating (slow surface) sausage modes in a magnetic pore, with a period range of 181–412 s, where a direct indication of wave energy dissipation was also observed. Furthermore, Keys et al. (2018) identified both surface and body sausage modes in several magnetic pores in the photosphere with frequencies in the range 2–12 mHz and mean energy fluxes of about 6–43 kW m^{-2} and 8 kW m^{-2}, respectively.

Area perturbations associated with MHD wave modes can more readily be measured in small-scale magnetic structures because the induced fractional variations in area are larger (e.g. small magnetic pores versus relatively large pores and sunspots). In addition to pores and sunspots, the identification of sausage modes in the lower solar atmosphere has been reported through a number of studies, for instance, in small (point-like) magnetic elements (Banerjee et al. 2001; Jain et al. 2014; Norton et al. 2021; Gao et al. 2021; Guevara Gómez et al. 2023), fibrillar structures (Morton et al. 2012; Gafeira et al. 2017; Sharma et al. 2018), and in coronal loops (e.g. Nakariakov et al. 2003; Aschwanden et al. 2004; Li et al. 2020).

In addition to sausage modes, transverse kink modes have often been simultaneously detected in a number of the above-mentioned studies (see also Stangalini et al. 2015; Jafarzadeh et al. 2017b). Some authors showed that both sausage and kink waves may readily coexist in the same magnetic concentration and can interact with each other by coupling their oscillatory motions (Jess et al. 2012; López Ariste et al. 2015).

Sausage modes are characterised by the contraction and expansion of a flux tube along its axis due to variations in the plasma density and magnetic field within the structure (e.g. a magnetic pore) as the wave passes along it (Roberts 1981). This results in periodic changes in the cross-sectional area of the magnetic concentration, which is often also associated with temperature fluctuations (Fujimura & Tsuneta 2009). These compressible waves are thought to contribute strongly to the heating of the upper solar atmosphere (Morton et al. 2012). On the other hand, kink modes involve oscillations of the magnetic field lines, causing the magnetic structure to oscillate transversely

(Spruit 1982). The (nearly) incompressible nature of the kink modes makes it relatively difficult to dissipate their energy compared to sausage modes (Braginskii 1965). Various mechanisms, including buffeting by and/or interacting with external granules (Evans & Roberts 1990; Hasan & Kalkofen 1999) and vortex-type photospheric drivers (Kitiashvili et al. 2011; Leonard et al. 2018), have been shown to excite sausage and kink modes in magnetic flux tubes.

While mode conversion can occur close to the plasma-$\beta \approx 1$ regions (i.e. where the gas and magnetic pressures nearly coincide; Bogdan et al. 2003; Cally 2007), the coupling between sausage and kink modes may also take place when one mode induces or excites the other (Roberts 2000; cf. Verwichte et al. 2006). For example, the compression and expansion associated with the sausage modes may cause a change in the equilibrium magnetic field configuration within the flux tube, leading to a perturbation of the magnetic field lines. This perturbation can then excite the kink modes. Conversely, the kink modes can also influence the sausage modes. The transverse oscillations induced by the kink modes can cause changes in the plasma pressure and magnetic tension within the flux tube, resulting in modifications to the contraction and expansion behaviour of the sausage modes. Furthermore, interaction between the various MHD wave modes in a flux tube can be complex, potentially leading to the excitation of higher-order wave modes, such as fluting modes, or to the modification of the existing modes. For example, an initially imposed kink mode in a thin flux-tube has been shown to excite a combination of sausage and fluting modes as part of the tube boundary perturbation (Ruderman & Petrukhin 2022). These couplings can affect the propagation characteristics, energy transfer, and damping rates of the oscillations within the flux tube. These various MHD wave modes, in particular, the fluting modes, may therefore suggest a complex interplay between the magnetic fields, plasma dynamics, and the surrounding environment. An identification of concurrent wave modes and their possible couplings is therefore essential for a better understanding of the dynamics and heating of the solar atmosphere. For a detailed mathematical description and further explanations of the various MHD wave modes, we refer to Roberts (2019).

In addition to the dependence on the size of the structure and spatial resolution of the observations, the identification of wave modes is affected by the variable seeing due to the Earth's atmosphere (Jess et al. 2021b). Seeing-free observations of (spatially resolved) small-scale magnetic structures from space can therefore better guarantee the absence of spurious signals and/or disturbances arising from the turbulence in the Earth atmosphere.

We analyse small magnetic pores in seeing-free, high-quality, and stable observations from the High Resolution Telescope (HRT; Gandorfer et al. 2018) of the Polarimetric and Helioseismic Imager (PHI; Solanki et al. 2020) on board the Solar Orbiter (Müller 2020) spacecraft. These small (but spatially resolved) magnetic structures were found to present area and horizontal-displacement fluctuations, which are ideal cases for studying MHD (sausage and kink) wave modes. Oscillations in various physical parameters, namely area, intensity, LOS velocity, and the longitudinal component of the magnetic field, were examined in four small (isolated) pores that were observed during the first perihelion of the nominal science phase of Solar Orbiter in March 2022. The POD techniques were employed to segregate the observed signals into constituent wave modes, where the associated plasma and oscillatory properties can be further characterised from the identified modes.

The observational data and their analyses are described in Sects. 2 and 3, respectively. Concluding remarks on the detected multiple wave modes are presented in Sect. 4.

2. Observations

The data we analysed were obtained by the Solar Orbiter/PHI-HRT during its first remote-sensing window of the nominal mission phase (Zouganelis et al. 2020) on 2022 March 7 between 00:00–00:45 UTC, with a cadence of 60 s and a spatial sampling of $0''\!.5$ per pixel (corresponding to 181 km on the solar surface at a distance of 0.501 au from the Sun). The observations captured active region AR12960, consisting of several sunspots and pores of different sizes and properties, located at a cosine of heliocentric angle (μ) of 0.87. The HRT sampled an entire field of view (FoV) of $370 \times 370\,\mathrm{Mm}^2$ in full Stokes, employing the magnetically sensitive Fe I 6173.34 Å line at six wavelength positions (five within the line and one in the continuum).

The full Stokes data, reduced on the ground (Sinjan et al. 2022), were corrected for optical aberrations introduced by the entrance window of the instrument without reconstructing for the diffraction at the entrance pupil (Kahil et al. 2022, 2023), resulting in a noise level of $\approx 1.8 \times 10^{-3}$ in Stokes Q/I_c and V/I_c, and $\approx 2.2 \times 10^{-3}$ in Stokes U/I_c, where I_c is the continuum intensity level. Furthermore, various physical parameters were inferred by means of Stokes inversions using the Milne-Eddington C-MILOS code (Orozco Suárez & Del Toro Iniesta 2007).

We analysed LOS velocities retrieved from the Stokes inversions, as well as circular polarisation (CP) as a measure of the longitudinal component of the magnetic field. The CP parameter was calculated as

$$\mathrm{CP} = \frac{1}{4}\left(\sum_{i=1}^{2} V_i - \sum_{i=4}^{5} V_i\right), \tag{1}$$

where V_i are the Stokes V parameters in the blue ($i = [1, 2]$) and red ($i = [4, 5]$) wings of the spectral line. The sign of the Stokes V in the red wing was changed to avoid cancellation of opposite polarities in the two wings (Martínez Pillet et al. 2011). The line-core position ($i = 3$) was excluded due to the presence of mixed polarities. Thus, the CP has a lower noise level (by about a factor of 2) than that from any single wavelength position in Stokes V.

For more information about these observations, their reduction and preparation procedures, and for a discussion of the preferred use of CP over the inferred magnetic field for wave studies, we refer to Calchetti et al. (2023), where the same dataset has been described in greater detail.

3. Analysis and results

We aimed to investigate oscillatory signals not only in intensity, LOS velocity, and CP, but particularly in the size (area) of magnetic structures. Only small-scale magnetic flux tubes may present these (measurable) large fractional area variations within a relatively short period of time (i.e. the 45 min length of the observation time-series). We focused on small magnetic pores in our observations that are large enough to be spatially resolved, but small enough to potentially show large fractional area variations.

Within the entire FoV of the active region (see Fig. 1 in Calchetti et al. 2023; also for the other data products) lie several pores of various sizes and properties. We found only four candidates that in addition to their small dimensions (with diameters of about 0.7 Mm) did not show any peculiar temporal evolution, such as interaction with neighbouring pores and/or other features over the course of the time series.

Figure 1 illustrates a small part of the Solar Orbiter/PHI-HRT FoV in both Stokes I continuum (left) and CP (right), in which the four pores of interest are marked with small squares and are numbered. The pores are present over the entire duration of the observations. However, pore 2 displays a complex evolution towards the end of the time series, and it was therefore analysed only over the first 37 min of the data set. Visual inspection of Fig. 1 indicates that the four pores are located in somewhat different magnetic environments, which can influence the local plasma flows (Ji et al. 2016). It is evident that pore 1 is the most isolated of our four features of interest. No other pores, sunspots, or even many plage patches are located nearby. Pores 2 and 3 are situated in the vicinity of other pores, and both are located in the middle of plage/enhanced-network regions, where inflows from opposite directions may have produced the relatively high number density of magnetic field concentrations in a small region. Finally, pore 4 is in a somewhat different situation compared to the other three. It is located in the immediate vicinity of a forming sunspot. From a close inspection of the image time-series, it is also evident that pore 4 moves the largest distance (towards the forming sunspot) of all pores. The other three pores have smaller spatial displacements. Furthermore, pore 1 has an opposite polarity compared to the other three features of interest. It is worth noting that continuum-intensity images are also essential for identifying these pores, in addition to magnetograms. For instance, pores 2–4 are located within plage (or enhanced-network) regions, and therefore, they could hardly be detected as a pore from the CP map alone.

Each pore was analysed separately within individually selected sub-fields of the FoV marked with red squares in Fig. 1. The boundary of the pores at each time step was determined by means of an active contour segmentation method, which was applied on inverted mean-subtracted intensity images (of the Stokes I continuum; brightness values were inverted to facilitate segmentation). The best contour levels were found to be about 60% of the maximum intensity (of the inverted mean-subtracted images). Slightly different contour (intensity) levels have no effect on the oscillatory signatures, but provide small changes in the absolute values of the internal areas. After we identified the boundaries (i.e. the sizes of the pores), the continuum intensity, LOS velocity, and CP values were also extracted at all pixels within the pore boundaries. We note that the LOS velocities in the four pores have a mean of $0.7\,\mathrm{km\,s^{-1}}$ and a standard deviation of $0.4\,\mathrm{km\,s^{-1}}$. This is well below the spectral sampling of Solar Orbiter/PHI (70 mÅ, equivalent to $\approx 3.4\,\mathrm{km\,s^{-1}}$), thus ensuring negligible influence on the CP measurements. Furthermore, we determined the centroid of each pore (the geometric centre of the pore) as the position of the magnetic structure at any given time, resulting in the calculation of (instantaneous) horizontal velocities of the pore over the length of the time series. The horizontal velocities were computed as transversal displacements of the pore within consecutive frames divided by the cadence of the observations. Together, these parameters provided us with the possibility of exploring the temporal evolution (fluctuations) in the area, horizontal velocity, mean intensity, mean LOS velocity, and mean CP of each pore (each of the latter three parameters were obtained as an average over the entire area of the pore). Since we are interested in wave signatures and not in the slow evolution of the pores, we subtracted low frequencies (<1 mHz) from all signals by means of wavelet filtering. All signals were also detrended (linearly) and apodised (using a Tukey window) prior to any further analyses.
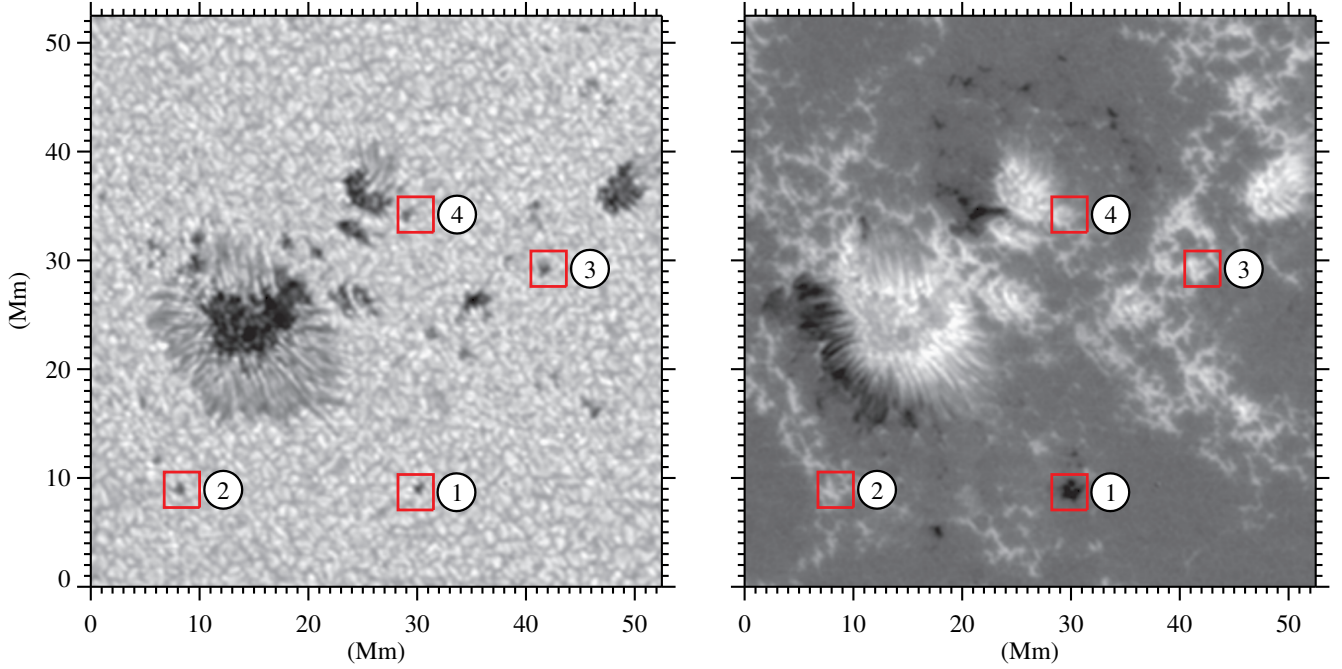
Fig. 1. Four small pores of interest marked on a Stokes *I* continuum image (left) and a CP map (right; with a range of $[-2.9, 5.7]\%$ in units of Stokes *I* continuum), corresponding to the middle of the time series.
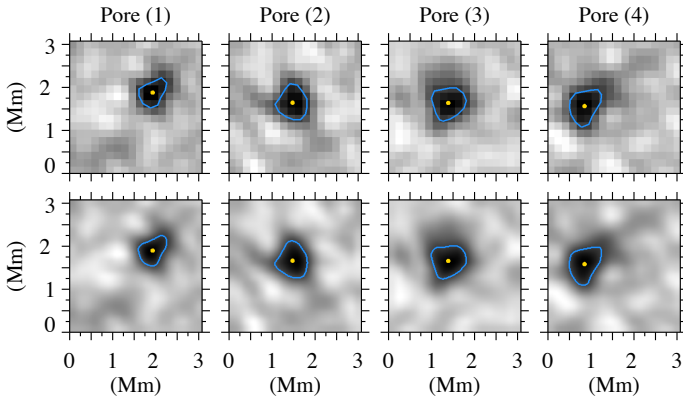

Fig. 2. Four pores of interest (in the Stokes *I* continuum) in the original spatial sampling (upper row) and in a higher sampling resolution (lower row) in the middle of the time series (as marked in Fig. 1). The solid blue contours depict the identified pore boundaries, and the yellow dots mark the centroid of the pores.

Figure 2 represents the four pores in the original spatial-sampling of the observations (upper row) and in a higher sampling resolution (increased by a factor of 10; using linear interpolations) for better visibility (lower row). We note that the analyses were performed on the original images, with the exception of modelling the boundary oscillations using the POD technique. Although the area oscillations are identical in both sets of spatial samplings (i.e. no effect on the modelling), the images with a higher sampling resolution facilitate mode identification through POD (see Sect. 3.2).

3.1. Perturbations in physical parameters

The temporal variations in the area, pore-averaged intensity, pore-averaged LOS velocity, and pore-averaged CP are displayed in Fig. 3 for the four pores of interest. Due to the high-pass frequency filtering, the original amplitudes might be slightly affected, even at high frequency. This does not affect the results because we are only interested in identifying oscillatory signals and their phase relations. All plots are therefore shown in arbitrary units. Moreover, we primarily studied area fluctuations in the small magnetic pores, which together with phase relations between other oscillatory signals can characterise the sausage and possibly the kink modes better.

Figure 4 presents refined global wavelet power spectra of the four observables shown in Fig. 3, combined for the four small pores (the four pores display similar power spectra for fluctuations in each of the observables). The refined global wavelet spectra are time-integrated power spectra that only include areas in the wavelet power spectrum (using a Morlet function; Torrence & Compo 1998) falling within the 95% confidence levels and outside of the cone of influence (CoI; subject to edge effects) of the wavelets. In other words, they represent the power-weighted frequency distributions of the wavelet with significant power, unaffected by the CoI. The oscillations in area, intensity, LOS velocity, and CP show a relatively wide frequency distributions with peaks at around 2.5, 2.3, 3.3, and 2.5 mHz, respectively. The small differences between the peaks could be representative of different MHD wave modes, similar to those found by Calchetti et al. (2023) in other (considerably larger) magnetic structures within the same active region from the same dataset (but using a different analysis approach).

The areas of the pores 1–4 have maximum variations (after detrending and high-pass filtering) of 33%, 54%, 39%, and 31%. The fact that we observe such large area oscillations most likely indicates the presence of sausage modes. Furthermore, we observe horizontal velocity perturbations (with frequencies of about 2–5 mHz) that are not artefacts produced by the spacecraft jitter because the various pores did not move in phase in (exactly) the same direction. Although these horizontal velocity fluctuations have relatively small amplitudes ($\approx 0.7\,\mathrm{km\,s^{-1}}$ on average),
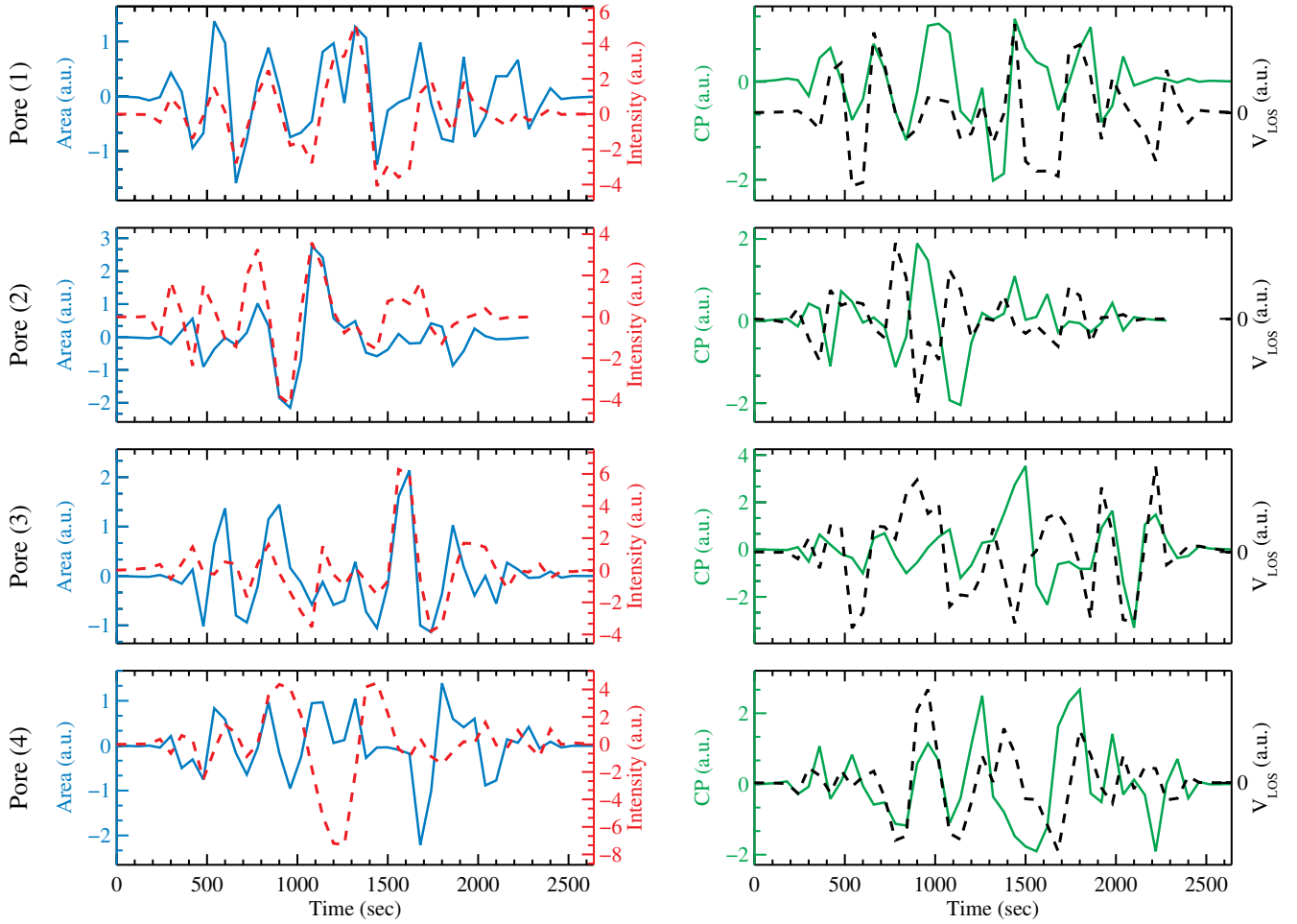
Fig. 3. Perturbations in various physical parameters of the four pores of interest. The left panels show the area (solid blue) and pore-averaged intensity (dashed red) fluctuations, and the pore-averaged CP (solid green) and pore-averaged LOS velocity (dashed black) oscillations are presented in the right panels. The plots in a given row show the results for one pore, as indicated left of the figure. All signals are detrended (linearly) and apodized (using a Tukey window). Low frequencies (<1 mHz) have been filtered out. The amplitudes are therefore not preserved and thus are all shown in arbitrary units (a.u.).

they may imply the presence of kink modes (these oscillations might be caused by the dynamics of the external flow, or they might be intrinsic to the pore).

To further examine these initial suggestions, we performed a modal analysis using the POD technique (Sect. 3.2), followed by a wavelet phase-lag analysis between pairs of oscillations observed in the various parameters (i.e. those shown in Fig. 3) in comparison with theoretical models (Sect. 3.3).

3.2. Proper orthogonal decomposition of pore boundary shapes

The large oscillations in pore areas, as shown in the previous Section 3.1, also naturally result in measurable changes in pore shape. In this section, we identify modes by analysing the change in the shape of the pore boundary with time. We decomposed this motion using POD. POD is an sophisticated data-driven method that can extract dominant wave modes by identifying spatial patterns and temporal dynamics of a structure that significantly contribute to its overall variability. More specifically, POD determines the eigenfunctions that are orthogonal in space. In this way, POD allows for the decomposition of a time series into spatial modes that are associated with a range of different frequencies or spectral bands.
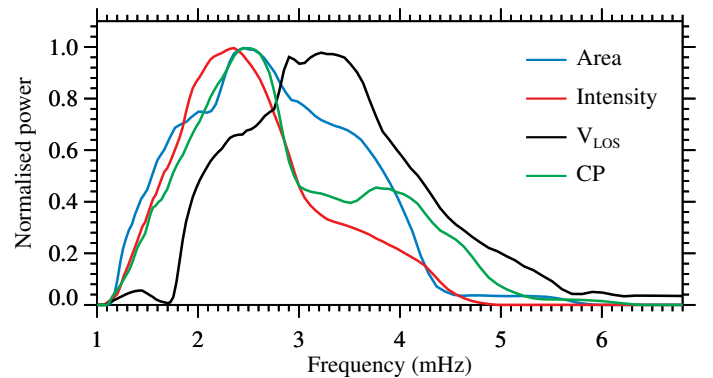

Fig. 4. Refined global wavelet power spectra of the four observables shown in Fig. 3 for the four small pores. The power spectra are normalised by their maximum value.

This powerful data-analysis method has been used to obtain a low-dimension approximation of a high-dimensional process. It was initially introduced in the context of fluid dynamics by Lumley (1967) to analyse coherent structures in turbulent flows. Only recently has its application on large solar magnetic structures (i.e. sunspots) been developed, where it allowed the
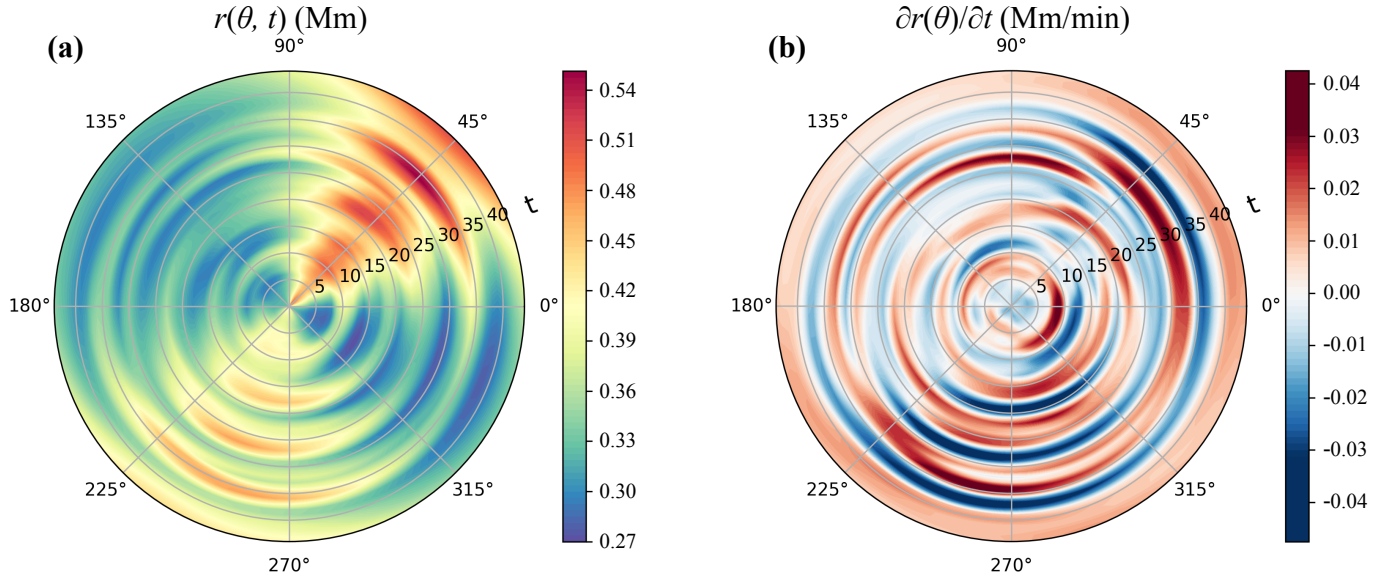
(a) $r(\theta, t)$ (Mm)

(b) $\partial r(\theta)/\partial t$ (Mm/min)

Fig. 5. Contour maps of the pore radial coordinates of pore 1 as a function of polar angle, θ, and time, t (a), and of $\partial r(\theta)/\partial t$ (b). The time variation is plotted on the radial axis (in minutes) for both contour maps.

identification of multiple high-order eigenmodes in the photosphere for the first time (Albidah et al. 2021, 2022). POD is a particularly useful modal decomposition for inhomogeneous unsteady flows or environments. Its fundamental idea is to decompose a set of fluctuation fields, the so-called snapshots, into a sum of orthonormal spatial modes organised (ranked) by their eigenvalues (or their contribution to the total variance). The higher the eigenvalue, the stronger the variance (or energy) that is captured by that mode. This means that POD modes with higher eigenvalues are more significant in terms of explaining the variability in the data. Thus, both spatial structure and temporal evolution of each POD (or empirical) mode are obtained.

Before we analyse the change in the shape of the pore boundaries with time to identify MHD wave modes, first we note that the oscillations of the pore centroids may be attributed to the movement of the external flows, which are highly non-stationary. For this reason, our analysis was carried out after shifting each pore centroid to the centre of the FoV (i.e. the origin of the system) in an attempt to isolate the movements of the pore boundary from the advective effects of the external flow field. Then, we extracted the x and y coordinates of the boundary (for each magnetic pore) at each time step for the entire duration of the observations and determined the distance between the coordinates of the boundary and the position of the centre. This helped us to transform the shape of the pore into a polar coordinate system (r, θ), interpolated into an equally spaced grid in the θ direction, with 360 points.

This process was repeated for all instances in time, generating a matrix that described the variation in the shape of the analysed pore as a function of time (i.e. $r(\theta, t)$), as displayed in Fig. 5a for pore 1. The plot illustrates the temporal variation in the size of the pore in all directions in polar coordinates for the whole duration of the time series. Each circle represents the size of the pore (i.e. the distance between the pore boundary and the pore centre) depicted in the background colour for all polar angles at a particular time step. Time starts at the centre of the circle going outwards, so that the radius of the disk is the time of observations. The resulting matrix is helpful for analysing the dynamical system and was used for the modal analysis of the pore.

Figure 5a shows that the background colour in the radial direction (representing the time variation of the pore radius) increases and decreases at all angles, showing that the pore expands and contracts (i.e. boundary oscillations). It is also evident that the fluctuation of the pore radius is not uniform in the θ direction, predominating (peaking) at around $\theta = 45°$ and $250°$. This may be related to a periodic movement of the centre of mass. We note that both the pore radius and the oscillation amplitude are larger in the abovementioned θ directions. In other words, the variation in the pore radius is larger in the directions in which the pore is more extended.

Figure 5b shows $\partial r(\theta)/\partial t$. This plot reveals regular contractions and expansions at all polar angles, and periods of about 7–10 min are linked to this oscillatory process. These matrices, containing the coordinates of the pore boundary, were used as input for the POD analysis. A snapshot here refers to the shape of the boundary of each pore at one moment in time (Fig. 5 represents a set of snapshots), and POD was able to compute as many empirical modes as there were time snapshots (i.e. 45). However, not all POD modes are physical. Many of them can be due to noise or spurious signals, for example. To identify which empirical modes describe MHD modes, the POD spatial modes were accordingly compared with those predicted by cylindrical flux-tube models (when the amplitudes of the POD modes are considerably larger than the noise levels). We therefore decomposed the radial coordinate of a pore boundary as

$$r(\theta, t) = \langle r(\theta) \rangle + r'(\theta, t) = \langle r(\theta) \rangle + \sum_{n=1}^{N} a^{(n)}(t)\,\phi^{(n)}(\theta), \qquad (2)$$

where $\phi^{(n)}$ represents a set of space-dependent orthonormal modes, $a^{(n)}$ is a time-dependent mode amplitude, N is the number of snapshots, and n identifies the mode index. Here, $\langle \rangle$ represents a time average, and the prime denotes a fluctuation. A reconstructed fluctuation field can then be approximated by

$$\tilde{r}'(\theta, t) \approx \sum_{n=1}^{M} a^{(n)}(t)\,\phi^{(n)}(\theta), \qquad (3)$$

where M is the number of modes used in the reconstruction. Using the snapshots method introduced by Sirovich (1987), we
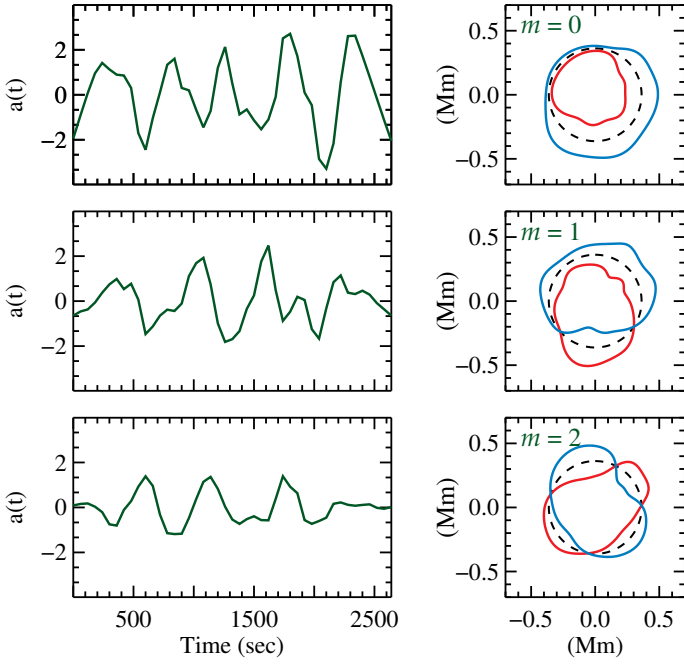
Fig. 6. POD modal analysis of pore 1. The left column illustrates the results of POD temporal modes, $a(t)$, for the first three modes (i.e. sausage, kink, and fluting modes, corresponding to the azimuthal wave numbers, $m = 0$, 1, and 2). The right column presents their corresponding spatial modes, $\phi(x, y)$ in a Cartesian coordinate system, projected over a reference circle. The blue and red curves show the maximum positive and negative values of the perturbations, respectively.

constructed the modal basis using a covariance matrix of the radius fluctuation field as

$$C_{t_1,t_2} = \frac{1}{N} \int_\Omega r'(\theta, t_1)\, r'(\theta, t_2)\, \mathrm{d}\theta. \tag{4}$$

This matrix is symmetric, positive, and semi-definite. We therefore computed the eigenvalues and eigenvectors using singular value decomposition (SVD). Thus, the POD spatial modes were computed by a linear combination of the snapshots into an orthonormal set of basis functions,

$$\phi^{(n)}(\theta) = \frac{1}{\lambda_n N} \sum_{k=1}^{N} \xi_{k,n} r'(\theta, t_k), \tag{5}$$

where λ_n are the eigenvalues, and $\xi_{k,n}$ represents the sets of eigenvectors of the correlation matrix C. The term k represents the kth column of ξ in the eigenvalue problem $C\xi = \lambda\xi$. Finally, the time-dependent mode amplitude is given by

$$a^{(n)}(t_k) = \sqrt{N\lambda_n}\, \xi_{k,n}. \tag{6}$$

Figure 6 illustrates the results of the modal analysis obtained by POD for pore 1. The left panels display the temporal evolution of the coefficients $a(t)$, and the right panels show their spatial structures for the first, second, and third POD modes (i.e. those with $n = 1$, 2, and 3). Only the first three POD modes were found to be reliable and physical as the other modes did not present an oscillatory time coefficient or their contribution to the overall signal was insignificant. The spatial perturbations, projected over a reference circle (depicted by the dashed black line), were retrieved from the following equations:

$$\begin{aligned} x &= (1 \pm r')\,\cos(\theta) = (1 \pm \phi)\,\cos(\theta), \\ y &= (1 \pm r')\,\sin(\theta) = (1 \pm \phi)\,\sin(\theta). \end{aligned} \tag{7}$$
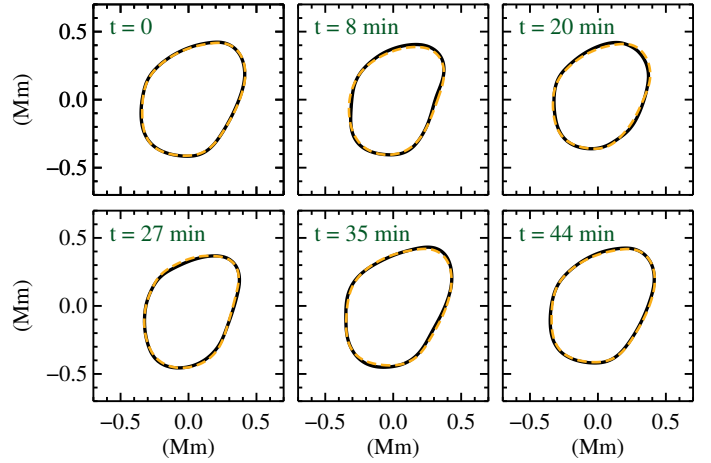

Fig. 7. Comparison between the boundary of pore 1 at different time steps. The solid black lines represent the boundary extracted from the observational data, and the dashed orange lines depict POD reconstructions using the first three POD modes.

The spatial modes are shown in blue for positive and in red for negative values of disturbances. The temporal coefficients of the first three empirical modes for pore 1 reveal harmonic perturbations with peak frequencies at 2 mHz, 1.7 mHz, and 1.8 mHz. The first mode is predominantly due to the (asymmetric) radial expansion and contraction of the pore in all directions, thus representing a sausage mode (the azimuthal wave number, $m = 0$) when compared with a cylindrical flux-tube model. The second mode is mainly related to the movement of the centre of mass along the y-axis, corresponding to a kink mode ($m = 1$). Finally, the third POD mode is primarily representative of a fluting wave mode ($m = 2$), according to the standard cylindrical flux-tube models. We note that the MHD modes were recognised by their primary mode characteristic, which refers to their main type of motion in our observations. It is important to note that the oscillatory movements seen in the pore cross-sections may not perfectly align with the expected movements for the eigenmodes of a cylindrical flux tube (which exhibits perfect symmetry in shape and oscillations). This discrepancy can be attributed not only to the irregular non-circular shapes of the observed wave guides, namely the small pores, but also to the asymmetric oscillations in the observations. This variation, however, does not significantly impact the overall agreement, or correlation, between the observed and theoretical wave modes. The identification of each MHD wave mode is determined by the best agreement obtained, indicating the most accurate match between them.

Figure 7 illustrates how the reconstructions of a pore boundary (i.e. its shape) at six selected time steps from the first three modes detected by POD (dashed orange curves) match the identified boundaries from the observations (solid black curves). It is evident that all the POD reconstructions agree well with the original data and almost perfectly capture the pore dynamics (for the first three empirical modes). It is worth noting again that POD is a data-driven technique and is therefore not limited to predefined eigenfunctions. POD was therefore able to reliably decompose MHD wave modes in the small pores with irregular cross-sectional shapes.

Figure 8 summarises the spatial structure of perturbations of the boundary of all four pores as a result of the POD analysis applied to the remaining three pores (for completeness, it also again includes those of pore 1). The three POD modes are organised into three columns from left to right, while the rows denote
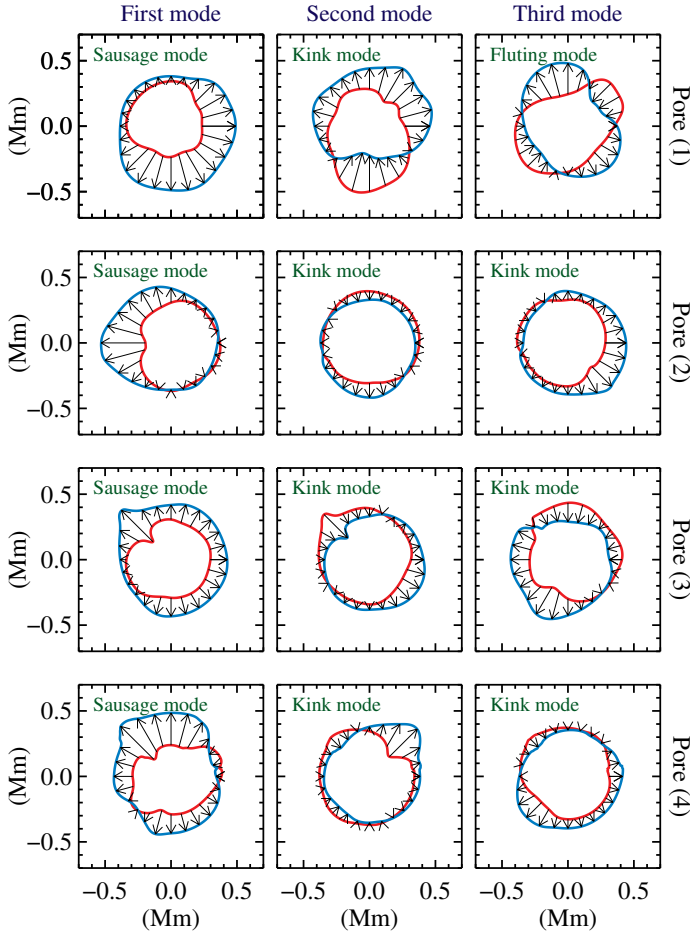
Fig. 8. Modal perturbations of the four pores of interest recovered by POD. From left to right, the three columns illustrate the first, second, and third POD modes (ranked by their eigenvalue magnitudes) of each pore in a separate row. The blue and red lines depict the maximum positive and negative values of perturbations, respectively. The arrows connect selected points from the red to blue curves to illustrate directions of motion within each half oscillation period. The identified eigenmodes are marked in the top left corner of all panels. For all four pores, the first and second modes represent the sausage and kink modes, respectively. The third mode revealed a fluting mode for pore 1 and kink modes for pores 2–4. The temporal evolution of the modes for each pore are available as online movies.

Table 1. Area percentage differences between the maximum negative and positive perturbations associated with the three wave modes in the four pores.

	First mode	Second mode	Third mode
Pore (1)	84%	28%	14%
Pore (2)	50%	2%	36%
Pore (3)	64%	7%	11%
Pore (4)	67%	9%	22%

Table 2. Oscillation frequency of the POD modes identified in the four pores.

	First mode	Second mode	Third mode
Pore (1)	2.0 mHz	1.7 mHz	1.8 mHz
Pore (2)	1.7 mHz	1.4 and 1.9 mHz	1.8 mHz
Pore (3)	3.0 mHz	2.3 mHz	2.7 mHz
Pore (4)	1.5 and 2.3 mHz	2.4 mHz	2.0 mHz

mixing), although these distinctions are not straightforward form the analysis of the boundary oscillations alone.

To better visualise the main dynamics of the oscillations, arrows connecting (equally distanced) selected points from negative to positive fluctuations (i.e. from the red to blue curves) are also depicted in Fig. 8. These arrows indicate that the sausage modes (i.e. the first POD mode) are associated with the (asymmetric) expansion of the wave guides as the predominant motion in all four pores, while some small (minor) distortions are also observed in the case of pores 2 and 4. Moreover, for all four magnetic structures, the percentage differences in the area between the maximum negative and positive perturbations (associated with the first mode) are larger than 50%. Table 1 lists the area percentage differences between the maximum negative and positive perturbations (i.e. between the blue and red curves in Fig. 8). In the case of kink modes (from the second and third POD modes), the main dynamics are characterised by (asymmetric) movement from one side to the other, while some partial expansions may also be observed in parts of some of the irregularly shaped wave guides (that do not dominate). Additionally, their size variations are considerably smaller than those in the sausage modes. Finally, the fluting mode (the third POD mode of pore 1) mainly displays oppositely directed motions along perpendicular lines, with relatively small size changes.

The refined global wavelet power spectra of the three POD modes for the four pores are shown in Fig. 9. Their dominant frequencies are summarised in Table 2.

Thus, the pores show slightly different dominant frequencies of the different modes. They lie within the ranges of 1.5–3.0 mHz for the sausage modes and 1.4–2.7 mHz for the kink modes (from the second and third POD modes), and in the frequency of 1.8 mHz for the single observed fluting mode. These differences in the frequencies of the same modes in the four pores can be attributed to several factors, such as the transversal size of the magnetic wave guide, the length of the waves, and the physical parameters that describe the state of the plasma (strength of the magnetic field, temperature, density, etc.).

Finally, the eigenvalues, λ_i, associated with each POD mode i, normalised by the total sum of all eigenvalues, $\Sigma_{i=1}^{N} \lambda_i$, based on which the POD modes were ranked, are presented in Fig. 10. This normalisation provides a metric for assessing the individual
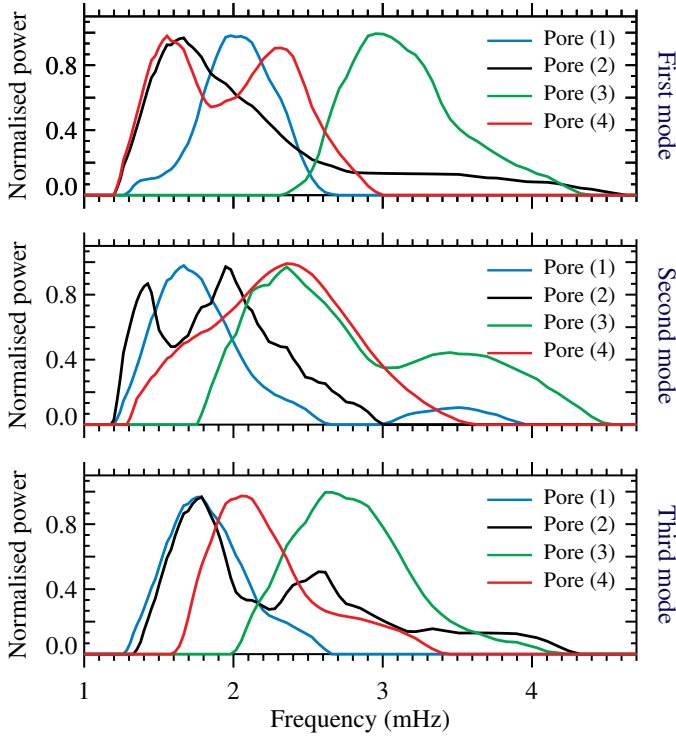
one of the four pores, as indicated on the right side of the figure. As in Fig. 6, the blue and red curves depict the positive and negative perturbation values, respectively. It is evident that for all the analysed pores, the sausage wave mode is the dominant POD mode, followed by the kink mode. Thus, the nature of the first two energetic modes (i.e. those with the highest eigenvalues) is the same as in the case of pore 1, but unlike pore 1, which showed a fluting mode, the third POD mode identified in pores 2–4 predominantly is a kink mode. This kink mode with its lower contribution (i.e. with a smaller variance; associated with the third POD mode) might be due to the non-circular cross-section of the structure. Furthermore, the variance observed between the two kink modes in each pore might be attributed to the difference in excitation strength. For example, granular buffeting might be stronger in one direction than in its perpendicular, which then excites kink modes with perpendicular polarisations. It is worth noting again that the MHD modes are identified by their main characteristics. However, the flavour of another wave mode may also be observed in some of the cases (e.g. as a result of mode

Fig. 9. Refined global wavelet power spectra of the first three modes obtained by POD for the four pores of interest.
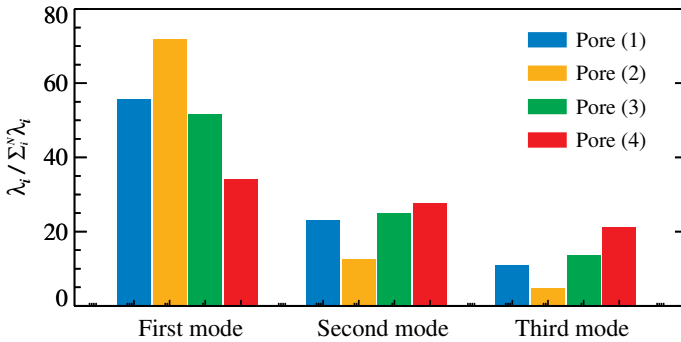

Fig. 10. Percentage of eigenvalues, λ_i, normalised by the total sum of all eigenvalues, $\Sigma_{i=1}^{N} \lambda_i$, of the first three POD modes. The first and second modes correspond to MHD sausage and kink modes for all pores, respectively. The third POD mode was identified as an MHD fluting mode for pore 1 and as kink modes for the other three pores.

contribution of each mode to the average variance or oscillation of the pore boundary. The oscillations observed in the shapes and areas of pores 1, 2, and 3 are mostly due to sausage modes, which cause 56%, 72%, and 52% of the pore dynamics, respectively. These are followed by kink modes with collective contributions (from the second and third POD modes) of about 23%, 17%, and 39% of the total eigenvalue, respectively. Pore 1 additionally receives a contribution from a fluting mode that is equal to 11%. For pore 4, however, the kink modes together dominate the sausage mode (49% of the total eigenvalue versus 34%, respectively).

3.3. Phase-lag analysis

Since the sausage modes were found to dominate the concurrent waves identified in the majority of the magnetic pores under

study (three out of four), we performed an additional investigation by means of a phase-lag analysis. Phase differences between perturbations in various pairs of observables may in comparison with theoretical models facilitate further characterisation of different sausage wave modes (see, e.g. Norton et al. 2021, for a recent similar analysis).

Using an MHD approach, Moreels & Van Doorsselaere (2013) determined the phase relations between various parameters, namely (flux-tube averaged) intensity, LOS velocity, and LOS magnetic field perturbations, in a uniform straight magnetic cylinder under solar photospheric conditions, with a particular focus on identifying different sausage modes. The various phase differences (summarised in Table 1 of their paper) might therefore suggest the presence of slow-propagating/standing or fast-propagating/standing surface modes. We used that table to investigate these characteristics in the four pores of interest studied here. Additionally, phase differences between area and intensity may reveal the slow or fast nature of the sausage modes, with in-phase relations indicating slow modes, and anti-phase specifying fast modes (Moreels et al. 2013).

We computed similar phase relations as in Moreels et al. (2013) and Moreels & Van Doorsselaere (2013). They were obtained by calculating a wavelet coherence spectrum and phase differences between oscillations in the pairs of observables, which are Area–Intensity, CP–V, V–Intensity, and Intensity–CP for each pore (V represents the LOS velocity; positive V indicates a redshift). From each wavelet coherence spectrum, the distribution of the phase lags was obtained in regions with significant coherence (i.e. significant at 5%; 95% confidence level) that are beyond the wavelet CoI. Figure 11 illustrates the distributions of te phase lag, φ, for $\varphi_{Area}-\varphi_{Intensity}$, $\varphi_{CP}-\varphi_V$, $\varphi_V-\varphi_{Intensity}$, and $\varphi_{Intensity}-\varphi_{CP}$, retrieved from the four pores. For each pore, only the phase relations associated with the peak frequencies of the sausage modes obtained from the POD analyses (with a window of 1 mHz) entered the histograms. Positive phase lags indicate that the first leads the second parameter (for details of the determination of phase differences from wavelet coherence spectra, see Jafarzadeh et al. 2017c). If no distribution is plotted for a particular pore in any of the phase relations, no significant coherence was found between the corresponding fluctuations in the pairs of observables.

A comparison between these phase lags and those predicted in Table 1 of Moreels & Van Doorsselaere (2013) obtained in the case of an ideal flux tube is not straightforward and should be interpreted with great caution. One reason are various phase lags (likely due to superposition of multiple wave modes in the same magnetic structure), so that a simple model may not account for a complex situation such as found in the real Sun. Additionally, the observed data may still contain noise and spurious signals that contribute to these phase differences. They are difficult to distinguish from real signals. Furthermore, the observables are likely formed at slightly different geometric heights. These height differences may additionally hinder the comparison of phase relations between the observed parameters and those from the theoretical models (which were calculated at the same geometric heights). Thus, we primarily aim to present the phase lags between the various observables and only attempt to tentatively make these comparisons for frequencies at which the sausage modes were identified by POD (i.e. those shown in Fig. 11).

The best agreement with the theoretical models developed by Moreels & Van Doorsselaere (2013) was found for the $\varphi_{CP}-\varphi_V$ and $\varphi_{Intensity}-\varphi_{CP}$ phase relations (from pores 4 and 3, respectively), implicating the identification of fast-propagating surface modes. Additionally, the $\varphi_{Intensity}-\varphi_{CP}$ relation (and to a lesser
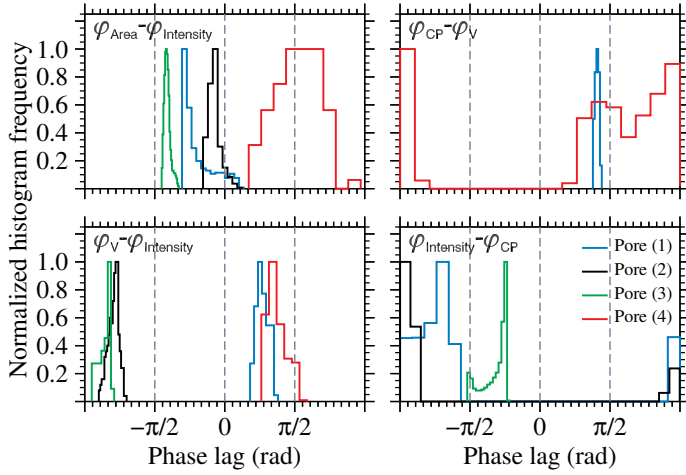
Fig. 11. Distributions of the phase lag for oscillations in four pairs of observables: Area–Intensity (top left), CP–LOS velocity (top right), LOS velocity–Intensity (bottom left), and Intensity–CP (bottom right), associated with the frequencies of the POD sausage modes. The histograms are normalised to their maximum values. The vertical lines mark phase lags of $-\pi/2$, 0, and $\pi/2$ radians.

extent, the $\varphi_{\text{Area}}-\varphi_{\text{Intensity}}$) for pore 2 suggested a slow sausage mode. However, since not all distributions can agree with those predicted by the models (see the previous paragraph for some possible reasons), these comparisons are not considered conclusive.

4. Discussion and conclusions

We have inspected the concurrent presence of MHD wave modes in small magnetic pores captured by Solar Orbiter/PHI-HRT under seeing-free observing conditions. While we studied perturbations in various observables, the focus was on analysing oscillations of the area and shape of the pores. The decomposition of these oscillations with the POD technique (for the first time, to our knowledge) has revealed the existence of concurrent sausage and kink modes in all four pores under investigation. More interestingly, we also identified a higher-order eigenmode, a fluting mode, in one of these small-scale magnetic structures.

The POD analysis resulted in different distributions of the eigenvalue for the four magnetic pores. While the dynamics in pores 1-3 was found to be dominated by the sausage modes, the kink modes contributed more to the total eigenvalue in pore 4. Moreover, the fluting mode was identified only in pore 1. These differences could likely be due to the different local plasma (and magnetic) environments in which the pores resided. It is worth noting that the embedded plasma flows in different sections of the same active region were shown to influence the kinematics of magnetic structures differently (Jafarzadeh et al. 2017a), so that they can affect the mode generation.

We note that the MHD wave modes are identified and interpreted by the dominant characteristic of each POD mode (as a result of decomposition of the boundary oscillations), that is, when their main motions are compared with cylindrical flux-tube models. However, the observed wave guides are shaped irregularly and may present multiple distortions while oscillating, as a result of inhomogeneous plasma inside and/or outside the magnetic structures or varying granulation buffeting from different angles, for example. Thus, each POD mode could also present a flavour of another MHD wave mode due to mode mixing, for instance, although this does not dominate. Each POD mode

might be a linear combination of MHD modes because the POD modal basis is estimated from the data themselves.

Although the characteristics of the local plasma, or magnetic environment, could be linked to the detected wave modes, we also note that these identifications might perhaps be influenced by several other factors, such as the spatial and temporal resolutions and the signal-to-noise ratio of the observations. In particular, while both the spatial and temporal resolutions can limit the detection of higher frequency fluctuations, the former may also create uncertainties in the pore boundary detection. The absence of other modes in our study therefore does not necessarily imply that they are not present in the pores we studied.

The most energetic mode in all four pores (i.e. that with the highest eigenvalue) was found to be the sausage mode, with frequencies in the interval 1.5–3.0 mHz. Even though these frequencies overlap, they are slightly lower on average than those reported in the literature for photospheric magnetic pores, for instance, 2.2–33.3 mHz (Morton et al. 2011), 2.4–5.5 mHz (Grant et al. 2015), and 2–12 mHz (Keys et al. 2018). Dorotovič et al. (2014) reported frequencies of 1.2–3.7 mHz in area perturbations of a large pore, which overlap most with those found here. However, we note that frequencies of the area perturbations do not necessarily represent the frequencies of sausage modes alone, but could also include other wave modes. This also implies that by assuming all variations in area to be due to sausage modes, the sausage mode energy is overestimated if the area changes are due to multiple wave modes.

The kink modes, as the second most energetic empirical mode (i.e. with the second highest eigenvalue) detected by POD was identified in a slightly smaller frequency range of 1.4–2.3 mHz (compared to that of sausage modes) in the four pores under study. Their frequencies are on the same order, but slightly lower, than the kink modes identified as the third empirical modes by POD (ranging between 1.8–2.7 mHz). The fluting mode was also found with a peak frequency at around 1.8 mHz. To the best of our knowledge, these are the first detections of kink and fluting modes in solar magnetic pores. The similar frequencies in the identified MHD wave modes may suggest that they are coupled to each other.

The second and third POD spatial modes for pores 2-4 represent kink modes with perpendicular fluctuation directions. This may provide an intriguing development in relation to the search for the signatures of torsional Alfvén waves in the solar atmosphere. Observations of Alfvén waves have long been sought due to their implications for atmospheric heating, but their incompressible nature makes a detection of the velocity excursions around a magnetic flux tube boundary due to their torsional oscillations difficult (Chelpanov & Kobanov 2022). Recent studies have reported torsional velocity signatures in magnetic structures as evidence of Alfvén waves (e.g. Srivastava et al. 2017; Kohutova et al. 2020; Stangalini et al. 2021b). However, the detection of orthogonal kink modes in this work implies that these modes in tandem may replicate the torsional behaviour of Alfvén waves (cf. kink wave's rotational motions may appear similar to those expected from torsional Alfvén waves, Goossens et al. 2014). It is vital to model the nature of these modes with realistic drivers (e.g. Kuźma et al. 2020; Riedl et al. 2021) to ascertain whether this kink mode interaction may influence the detection of Alfvénic motions in the solar atmosphere, in particular, for pores in which the kink modes dominate the sausage mode.

The large variations in pore area, up to 40 ± 10%, may suggest a non-linear regime. The most likely interpretation of this is a fast sausage mode according to the criteria developed by Moreels et al. (2013). The non-linear generation of fluting

perturbations by kink modes has previously been predicted in both straight and twisted magnetic flux tubes (Ruderman 2017; Terradas et al. 2018; Ruderman & Petrukhin 2022). However, we note that higher-resolution observations are needed to clarify both the non-linearity and fast and/or surface nature of the sausage modes in these small-scale magnetic structures.

To summarise, the concurrent sausage, kink, and fluting modes in photospheric small-scale magnetic structures have reliably been identified in the seeing-free data from Solar Orbiter/PHI-HRT. Understanding the behaviour and properties of these various MHD wave modes can provide us with valuable insights into the energy transfer mechanisms and the intricate dynamic processes occurring in the solar photosphere. The application of POD to CP and LOS velocity oscillations in the inner structure of the pores might quantify their specifications better. This is the subject of a forthcoming article. In addition, the propagation of the detected wave modes into the upper solar atmosphere needs further investigations using multi-height and multi-instrument diagnostics. Furthermore, we note that both POD and phase-lag analyses would greatly benefit from (a) observations with a higher spatial- and temporal-resolution that resolve the physical parameters within the magnetic structures spatially and temporally, and (b) a higher accuracy in the inference of the parameters, such as the magnetic field and LOS velocity (i.e. with a higher spectral sampling and resolution). In future studies, we therefore hope to conduct similar analyses on higher resolution observations (from, e.g. the next flight of the SUNRISE balloon-borne solar observatory; Solanki et al. 2010, 2017) as well as on MHD simulations. Additionally, longer seeing-free observations from Solar Orbiter/PHI-HRT in future observing campaigns (resulting in a higher frequency resolution) as well as future improvements on the HRT data-reduction routines (thus, a lower noise level) are essential for identifying more MHD wave modes. More importantly, the spatial resolution of Solar Orbiter/PHI-HRT during the second (and subsequent) perihelion passes will be up to 60% higher (minimum distance from the Sun ≤0.3 au) than those analysed here (where the spacecraft was at about 0.5 au during this first perihelion passage).

References

Albidah, A. B., Brevis, W., Fedun, V., et al. 2021, Phil. Trans. R. Soc. London Ser. A, 379, 20200181
Albidah, A. B., Fedun, V., Aldhafeeri, A. A., et al. 2022, ApJ, 927, 201
Albidah, A. B., Fedun, V., Aldhafeeri, A. A., et al. 2023, ApJ, 954, 30
Aschwanden, M. J., Nakariakov, V. M., & Melnikov, V. F. 2004, ApJ, 600, 458
Banerjee, D., O'Shea, E., Doyle, J. G., & Goossens, M. 2001, A&A, 371, 1137
Bate, W., Jess, D. B., Nakariakov, V. M., et al. 2022, ApJ, 930, 129
Bogdan, T. J., Carlsson, M., Hansteen, V. H., et al. 2003, ApJ, 599, 626
Braginskii, S. I. 1965, Rev. Plasma Phys., 1, 205
Calchetti, D., Stangalini, M., Jafarzadeh, S., et al. 2023, A&A, 674, A109 (SO Nominal Mission Phase SI)
Cally, P. S. 2007, Astron. Nachr., 328, 286
Chelpanov, A., & Kobanov, N. 2022, Sol. Phys., 297, 154
Dorotovič, I., Erdélyi, R., Freij, N., Karlovský, V., & Márquez, I. 2014, A&A, 563, A12
Edwin, P. M., & Roberts, B. 1983, Sol. Phys., 88, 179
Erdélyi, R., & Morton, R. J. 2009, A&A, 494, 295
Evans, D. J., & Roberts, B. 1990, ApJ, 348, 346
Feng, S., Deng, Z., Yuan, D., Xu, Z., & Yang, X. 2020, RAA, 20, 117
Freij, N., Dorotovič, I., Morton, R. J., et al. 2016, ApJ, 817, 44
Fujimura, D., & Tsuneta, S. 2009, ApJ, 702, 1443
Gafeira, R., Jafarzadeh, S., Solanki, S. K., et al. 2017, ApJS, 229, 7
Gandorfer, A., Grauf, B., Staub, J., et al. 2018, in Space Telescopes and Instrumentation 2018: Optical, Infrared, and Millimeter Wave, eds. M. Lystrup, H. A. MacEwen, G. G. Fazio, et al., SPIE Conf. Ser., 10698, 106984N
Gao, Y., Li, F., Li, B., et al. 2021, Sol. Phys., 296, 184
Gilchrist-Millar, C. A., Jess, D. B., Grant, S. D. T., et al. 2021, Phil. Trans. R. Soc. London Ser. A, 379, 20200172
Goossens, M., Soler, R., Terradas, J., Van Doorsselaere, T., & Verth, G. 2014, ApJ, 788, 9
Grant, S. D. T., Jess, D. B., Moreels, M. G., et al. 2015, ApJ, 806, 132
Grant, S. D. T., Jess, D. B., Stangalini, M., et al. 2022, ApJ, 938, 143
Guevara Gómez, J. C., Jafarzadeh, S., Wedemeyer, S., et al. 2023, A&A, 671, A69
Hasan, S. S., & Kalkofen, W. 1999, ApJ, 519, 899
Houston, S. J., Jess, D. B., Keppens, R., et al. 2020, ApJ, 892, 49
Jafarzadeh, S., Solanki, S. K., Cameron, R. H., et al. 2017a, ApJS, 229, 8
Jafarzadeh, S., Solanki, S. K., Gafeira, R., et al. 2017b, ApJS, 229, 9
Jafarzadeh, S., Solanki, S. K., Stangalini, M., et al. 2017c, ApJS, 229, 10
Jain, R., Gascoyne, A., Hindman, B. W., & Greer, B. 2014, ApJ, 796, 72
Jefferies, S. M., McIntosh, S. W., Armstrong, J. D., et al. 2006, ApJ, 648, L151
Jess, D. B., Pascoe, D. J., Christian, D. J., et al. 2012, ApJ, 744, L5
Jess, D. B., Morton, R. J., Verth, G., et al. 2015, Space. Sci. Rev., 190, 103
Jess, D. B., Van Doorsselaere, T., Verth, G., et al. 2017, ApJ, 842, 59
Jess, D. B., Snow, B., Houston, S. J., et al. 2020, Nat. Astron., 4, 220
Jess, D. B., Keys, P. H., Stangalini, M., & Jafarzadeh, S. 2021a, Phil. Trans. R. Soc. London Ser. A, 379, 20200169
Jess, D. B., Snow, B., Fleck, B., Stangalini, M., & Jafarzadeh, S. 2021b, Nat. Astron., 5, 5
Jess, D. B., Jafarzadeh, S., Keys, P. H., et al. 2023, Liv. Rev. Sol. Phys., 20, 1
Ji, K.-F., Xiong, J.-P., Xiang, Y.-Y., et al. 2016, RAA, 16, 78
Kahil, F., Gandorfer, A., Hirzberger, J., et al. 2022, in Space Telescopes and Instrumentation 2022: Optical, Infrared, and Millimeter Wave, eds. L. E. Coyle, S. Matsuura, & M. D. Perrin, SPIE Conf. Ser., 12180, 121803F
Kahil, F., Gandorfer, A., Hirzberger, J., et al. 2023, A&A, 675, A61 (SO Nominal Mission Phase SI)
Keys, P. H., Morton, R. J., Jess, D. B., et al. 2018, ApJ, 857, 28
Khomenko, E., & Collados, M. 2015, Liv. Rev. Sol. Phys., 12, 6
Kitiashvili, I. N., Kosovichev, A. G., Mansour, N. N., & Wray, A. A. 2011, ApJ, 727, L50
Kohutova, P., Verwichte, E., & Froment, C. 2020, A&A, 633, L6
Kuźma, B., Wójcik, D., Murawski, K., Yuan, D., & Poedts, S. 2020, A&A, 639, A45
Leonard, A. J., Mumford, S. J., Fedun, V., & Erdélyi, R. 2018, MNRAS, 480, 2839
Li, B., Antolin, P., Guo, M. Z., et al. 2020, Space. Sci. Rev., 216, 136

López Ariste, A., Luna, M., Arregui, I., Khomenko, E., & Collados, M. 2015, A&A, 579, A127

Lumley, J. L. 1967, Atmospheric Turbulence and Wave Propagation (Moscow: Nauka), 166

Martínez Pillet, V., Del Toro Iniesta, J. C., Álvarez-Herrero, A., et al. 2011, Sol. Phys., 268, 57

Moreels, M. G., & Van Doorsselaere, T. 2013, A&A, 551, A137

Moreels, M. G., Goossens, M., & Van Doorsselaere, T. 2013, A&A, 555, A75

Moreels, M. G., Freij, N., Erdélyi, R., Van Doorsselaere, T., & Verth, G. 2015, A&A, 579, A73

Morton, R. J., Erdélyi, R., Jess, D. B., & Mathioudakis, M. 2011, ApJ, 729, L18

Morton, R. J., Verth, G., Jess, D. B., et al. 2012, Nat. Commun., 3, 1315

Morton, R. J., Verth, G., Fedun, V., Shelyag, S., & Erdélyi, R. 2013, ApJ, 768, 17

Müller, D., St. Cyr, O. C., Zouganelis, I., , et al. 2020, A&A, 642, A1

Nakariakov, V. M., & Verwichte, E. 2005, Liv. Rev. Sol. Phys., 2, 3

Nakariakov, V. M., Melnikov, V. F., & Reznikova, V. E. 2003, A&A, 412, L7

Norton, A. A., Stutz, R. B., & Welsch, B. T. 2021, Phil. Trans. R. Soc. London Ser. A, 379, 20200175

Orozco Suárez, D., & Del Toro Iniesta, J. C. 2007, A&A, 462, 1137

Riedl, J. M., Gilchrist-Millar, C. A., Van Doorsselaere, T., Jess, D. B., & Grant, S. D. T. 2021, A&A, 648, A77

Roberts, B. 1981, Sol. Phys., 69, 39

Roberts, B. 2000, Sol. Phys., 193, 139

Roberts, B. 2019, MHD waves in the Solar Atmosphere (Cambridge, United Kingdom: Cambridge University Press)

Ruderman, M. S. 2017, Sol. Phys., 292, 111

Ruderman, M. S., & Petrukhin, N. S. 2022, Sol. Phys., 297, 116

Rutten, R. J., & Krijger, J. M. 2003, A&A, 407, 735

Sharma, R., Verth, G., & Erdélyi, R. 2018, ApJ, 853, 61

Sinjan, J., Calchetti, D., Hirzberger, J., et al. 2022, SPIE Conf. Ser., 12189, 121891J

Sirovich, L. 1987, Q. Appl. Math., 45, 561

Solanki, S. K., Barthol, P., Danilovic, S., et al. 2010, ApJ, 723, L127

Solanki, S. K., Riethmüller, T. L., Barthol, P., et al. 2017, ApJS, 229, 2

Solanki, S. K., del Toro Iniesta, J. C., Woch, J., et al. 2020, A&A, 642, A11

Spruit, H. C. 1982, Sol. Phys., 75, 3

Srivastava, A. K., Shetye, J., Murawski, K., et al. 2017, Sci. Rep., 7, 43147

Stangalini, M., Del Moro, D., Berrilli, F., & Jefferies, S. M. 2011, A&A, 534, A65

Stangalini, M., Giannattasio, F., & Jafarzadeh, S. 2015, A&A, 577, A17

Stangalini, M., Jafarzadeh, S., Ermolli, I., et al. 2018, ApJ, 869, 110

Stangalini, M., Baker, D., Valori, G., et al. 2021a, Phil. Trans. R. Soc. London Ser. A, 379, 20200216

Stangalini, M., Erdélyi, R., Boocock, C., et al. 2021b, Nat. Astron., 5, 691

Stangalini, M., Jess, D. B., Verth, G., et al. 2021c, A&A, 649, A169

Stangalini, M., Verth, G., Fedun, V., et al. 2022, Nat. Commun., 13, 479

Tarbell, T. D., Peri, M., Frank, Z., Shine, R., & Title, A. M. 1988, in Seismology of the Sun and Sun-Like Stars, ed. E. J. Rolfe, ESA Spec. Pub., 286, 315

Terradas, J., Magyar, N., & Van Doorsselaere, T. 2018, ApJ, 853, 35

Title, A. M., Tarbell, T. D., Topka, K. P., et al. 1989, ApJ, 336, 475

Torrence, C., & Compo, G. P. 1998, Bull. Am. Meteorol. Soc., 79, 61

Verwichte, E., Foullon, C., & Nakariakov, V. M. 2006, A&A, 446, 1139

Zouganelis, I., De Groof, A., Walsh, A. P., et al. 2020, A&A, 642, A3